A Novel Acceleration Algorithm for the Computation of Scattering From Two-Dimensional Large-Scale Perfectly Conducting Random Rough Surfaces with the Forward-Backward Method

Danai Torrungrueng, *Member, IEEE*, Hsi-Tseng Chou, *Member, IEEE*, and Joel T. Johnson, *Member, IEEE*

***Abstract*—The forward–backward method with a novel spectral acceleration algorithm (FB/NSA) has been shown to be an extremely efficient iterative method of moments (MoM) for the computation of scattering from one-dimensional (1-D) perfect electric conducting (PEC) and impedance rough surfaces [1]. The NSA algorithm is employed to rapidly compute interactions between widely separated points in the conventional FB method and is based on a spectral domain representation of source currents and the associated Green's function. For fixed surface roughness statistics, the computational cost and memory storage of the FB/NSA method are $\mathcal{O}(N_{tot})$ as the surface size increases, where N_{tot} is the total number of unknowns to be solved. This makes studies of scattering from large surfaces, required in low grazing-angle scattering problems, tractable. In this paper, the FB/NSA method is extended to analyze scattering from two-dimensional (2-D) rough surfaces. The NSA algorithm for this case involves a double spectral integral representation of source currents and the 3-D free-space scalar Green's function. The coupling between two spectral variables makes the problem more challenging, and the efficiency improvements obtained for 2-D surfaces are appreciable but not as dramatic as those for 1-D surfaces. However, the computational efficiency of the FB/NSA method for 2-D rough surfaces remains $\mathcal{O}(N_{tot})$ as one of the surface dimensions increases. Comparisons of numerical results between the conventional FB method and the FB/NSA method for large-scale PEC rough surfaces show that the latter yields identical results to the former with a reduction of CPU time and only a slight increase in memory storage. In addition, the numerical results of FB/NSA method are in good agreement with experimental data obtained from the University of Washington, Seattle, WA.**

***Index Terms*—Forward-backward method, novel spectral acceleration algorithm, tough surfaces.**

I. Introduction

ELECTROMAGNETIC (EM) wave scattering from random rough surfaces has been studied extensively, and several approximate analytical methods have been developed. At present, scattering from surfaces whose properties render the analytical theories invalid can be accurately calculated only through the use of numerical methods. The most commonly used technique is the surface integral equation approach, and its solution by the method of moments (MoM) [2]–[4]. Standard factorization techniques of the system matrix, such as LU decomposition, become intractable as the number of unknowns N_{tot} increases because of their computational complexity of $\mathcal{O}(N_{tot}^3)$. In addition, the standard MoM also requires memory storage of $\mathcal{O}(N_{tot}^2)$ to store all elements of a dense impedance matrix. To increase computational efficiency in solving the surface integral equation, several efficient methods based on iterative versions of the MoM have been developed. One iterative MoM, termed the forward-backward (FB) method, has been shown in many cases to provide a more rapid convergence than standard CG-like iterative algorithms [1], [5]–[8]. This method is functionally identical to the method of ordered multiple interaction (MOMI) [9], [10] and has been shown to be an $\mathcal{O}(N_{tot}^2)$ algorithm. Due to its rapidly-convergent property, it is worthwhile to determine ways to improve its computational efficiency.

Previous use of the FB method has emphasized the one-dimensional (1-D) problem. To improve the computational efficiency of the 1-D FB (MOMI) method, the novel spectral acceleration (NSA) algorithm has been used [1]. In this method, a neighborhood distance around each receiving element on the surface is defined to separate the strong interaction regions from the weak interaction regions. Direct matrix-vector multiplication is performed when the source points are in the strong interaction regions. The NSA algorithm is employed to rapidly compute weak interactions between widely separated points in the conventional FB method and is based on a spectral domain representation of source currents and the associated Green's function. For fixed surface roughness statistics, it can be shown that the computational cost and memory storage requirement of the FB/NSA method is $\mathcal{O}(N_{tot})$ as the surface size increases. Although previously applied exclusively with the FB method, the NSA algorithm can be easily incorporated into other iterative techniques as well.

The FB method for two-dimensional (2-D) rough surfaces has previously been studied by Tran [10], again using an $\mathcal{O}(N_{tot}^2)$ algorithm. In this paper, the FB/NSA method is extended from 1-D to 2-D random rough surface scattering (RRSS), and em-

Manuscript received August 27, 1999; revised March 10, 2000.

D. Torrungrueng and J. T. Johnson are with The Department of Electrical Engineering, ElectroScience Laboratory, The Ohio State University, Columbus, OH 43212 USA (e-mail: torrungd@ee.eng.ohio-state.edu; johnson@ee.eng.ohio-state.edu).

H.-T. Chou is with the Department of Electrical Engineering, Yuan Ze University, Chung-Li, Taiwan, R.O.C. (e-mail: hchou@saturn.yzu.edu.tw).

Publisher Item Identifier S 0196-2892(00)05897-6.

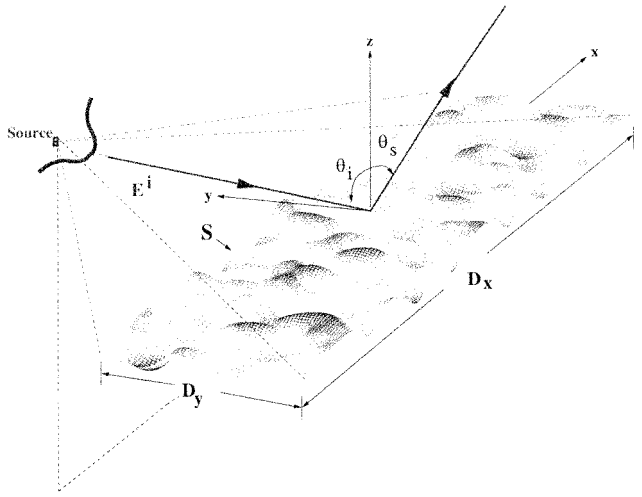

Fig. 1. Two-dimensional (2-D) PEC rough surface profile S illuminated by a *tapered* incident field $\boldsymbol{E}^i(x, y, z)$ centered in direction $\hat{k}_i = \hat{x} \sin\theta_i \cos\phi_i + \hat{y} \sin\theta_i \sin\phi_i - \hat{z} \cos\theta_i$.

ployed to perform matrix-vector multiplies for weak group interaction. The NSA algorithm for this case involves a double spectral integral representation of source currents and the three-dimensional (3-D) free space scalar Green's function. The coupling between two spectral variables makes the problem more challenging, and the efficiency improvements obtained for 2-D surfaces are appreciable but not as dramatic as those for 1-D surfaces. However, the computational efficiency of the FB/NSA method for 2-D RRSS remains $\mathcal{O}(N_{tot})$ as one of the surface dimensions increases. The FB/NSA method is specifically designed for 2-D large-scale finite rectangular surfaces and remains very efficient for moderately-rough, large-scale surfaces. Use of a large rectangular surface makes the method well suited for studying RRSS at low grazing angles (LGA) [11] and also for studies of backscattering enhancement [12].

In the next section, the FB method for 2-D RRSS is described. The formulation of the FB/NSA method is presented in detail in Section III. In Section IV, the computational cost and memory storage requirements of the FB/NSA method are discussed. Results and discussions are provided in Section V, and Section VI presents conclusions. An $e^{-i\omega t}$ harmonic time convention is assumed and suppressed throughout, and the propagation constant is defined as $k = \omega\sqrt{\mu\epsilon}$, where ω is the radian frequency, and ϵ and μ are the permittivity and permeability of free space, respectively.

II. Forward–Backward Method for 2-D RRSS

Consider a 2-D PEC rough surface profile S illuminated by an incident field $\boldsymbol{E}^i(x, y, z)$ centered in direction $\hat{k}_i = \hat{x} \sin\theta_i \cos\phi_i + \hat{y} \sin\theta_i \sin\phi_i - \hat{z} \cos\theta_i$, as shown in Fig. 1. The surface height function $z = f(x, y)$ has zero mean, and its maximum and minimum height variations are denoted by $z_{\max}$ and $z_{\min}$, respectively. The incident field $\boldsymbol{E}^i(x, y, z)$ is tapered with a Gaussian beam amplitude pattern confining the illuminated rough surface to the rectangular surface area $D_x \times D_y$ so that surface edges do not contribute strongly to obtained scattered fields, as described in [13].

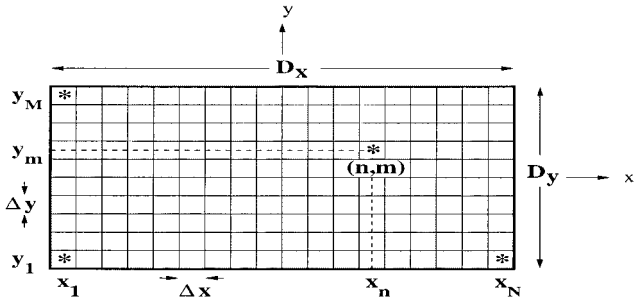

Fig. 2. Discretization of a rectangular surface area $D_x \times D_y$ of S_{xy} into an $N \times M$ rectangular grid. Each grid cell has the dimension $\Delta x \times \Delta y$.

Let $\boldsymbol{r} = \hat{x}x + \hat{y}y + \hat{z}z$ and $\boldsymbol{r}' = \hat{x}x' + \hat{y}y' + \hat{z}z'$ denote a field point and a source point on the rough surface, respectively. Then, the magnetic field integral equation (MFIE) on the PEC rough surface is given by

$$\boldsymbol{J}(\boldsymbol{r}) = \boldsymbol{J}_{PO}(\boldsymbol{r}) + 2\boldsymbol{n} \times \iint_{PV,\, S_{xy}} dx'\, dy'\, \nabla\, g(\boldsymbol{r}, \boldsymbol{r}') \times \boldsymbol{J}(\boldsymbol{r}') \tag{1}$$

where the above integral is a principal-value integral

$$\nabla\, g(\boldsymbol{r}, \boldsymbol{r}') = G(R)\boldsymbol{R} \tag{2}$$

$$G(R) = \frac{e^{ikR}}{4\pi R^2}\left(ik - \frac{1}{R}\right) \tag{3}$$

$\boldsymbol{J}(\boldsymbol{r}) = \boldsymbol{n} \times \boldsymbol{H}(\boldsymbol{r})$, $\boldsymbol{J}_{PO}(\boldsymbol{r}) = 2\boldsymbol{n} \times \boldsymbol{H}^i(\boldsymbol{r})$, $\boldsymbol{n} = \hat{z} - \hat{x}(\partial f/\partial x) - \hat{y}(\partial f/\partial y)$, $\boldsymbol{R} = \boldsymbol{r} - \boldsymbol{r}'$, and $R = |\boldsymbol{R}|$, where $\boldsymbol{H}^i$ is the incident magnetic field associated with $\boldsymbol{E}^i$. The normal vector $\boldsymbol{n}$ points upward from the PEC surface, and S_{xy} is the surface obtained from the projection of the rough surface S onto the xy plane. As usual, this surface integral equation can be solved using a standard point-matching MoM technique [2].

For the purpose of the MoM formulation, the rectangular surface area $D_x \times D_y$ of S_{xy} is discretized into the $N \times M$ rectangular grid, as shown in Fig. 2. Each (n, m)th element has the dimension $\Delta x \times \Delta y$, and its center is located at (x_n, y_m) in the coordinate system, where $n = 1, \cdots, N$ and $m = 1, \cdots, M$. Let $N_{tot} = 2NM$ be the total number of unknowns on the surface S [due to two independent components for $\boldsymbol{J}(\boldsymbol{r})$]. Using pulse basis functions and delta testing functions (i.e., point matching), the above MFIE can be discretized into the following MoM matrix equation:

$$\overline{\overline{Z}}\,\overline{I} = \overline{V} \tag{4}$$

where

$\overline{\overline{Z}}$ $N_{tot} \times N_{tot}$ MoM impedance matrix;
$\overline{V}$ $N_{tot} \times 1$ excitation vector;
$\overline{I}$ $N_{tot} \times 1$ solution vector.

Using pulse basis functions, point matching, and a *linear* surface model (no surface curvatures), it can be shown that the principal-value integration over the self (n, m)th element S_{self} vanishes

$$2\boldsymbol{n} \times \iint_{PV,\, S_{self}} dx'\, dy'\, G(R)\boldsymbol{R} \times \boldsymbol{J}(\boldsymbol{r}') = \boldsymbol{0}. \tag{5}$$

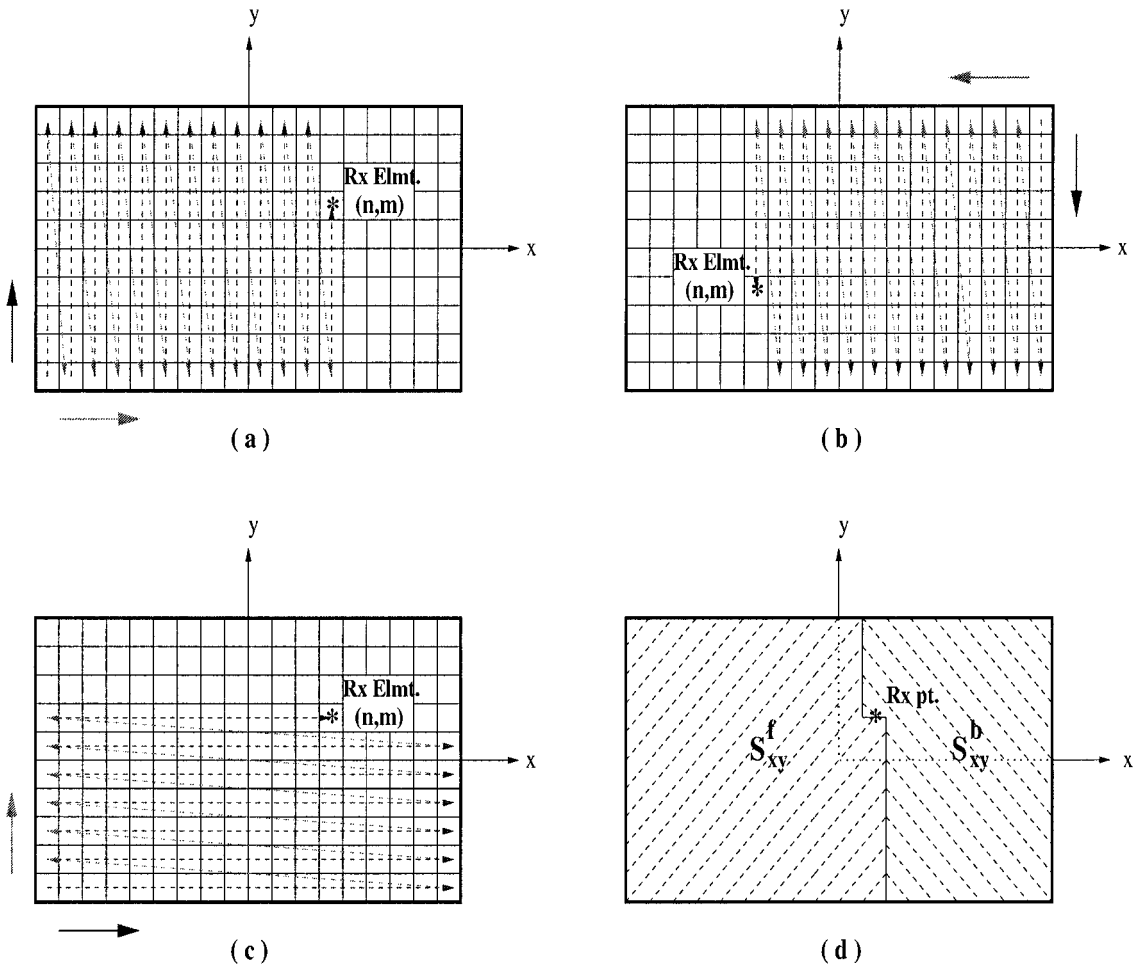

Fig. 3. Forward-stepping (FS) and backward-stepping (BS) processes. (a) FS process, (b) BS process, (c) alternative FS process, and (d) FS and BS projected surfaces.

To develop the FB method for the 2-DRRSS, it is desirable to make the following decomposition for the current vector $\boldsymbol{J}(\boldsymbol{r})$:

$$\boldsymbol{J}(\boldsymbol{r}) = \boldsymbol{J}^f(\boldsymbol{r}) + \boldsymbol{J}^b(\boldsymbol{r}) \tag{6}$$

where $\boldsymbol{J}^f(\boldsymbol{r})$ and $\boldsymbol{J}^b(\boldsymbol{r})$ are the forward-stepping (FS) and backward-stepping (BS) currents, respectively. The FS and BS processes as described in Tran [10] are illustrated in Fig. 3(a) and (b), respectively. For the FS process as shown in Fig. 3(a), the procedure starts from the (x_1, y_1) current element and moves from bottom to top and then from left to right until reaching the (x_n, y_m) current element, called the receiving element hereinafter. For the BS process, the sweep starts from the (x_N, y_M) current element and moves from top to bottom and then from right to left until reaching the receiving element, as shown in Fig. 3(b). It should be mentioned that these stepping processes can be defined differently. For example, for the FS process, one may start from the (x_1, y_1) current element and move from left to right first and then from bottom to top, as illustrated in Fig. 3(c). However, for the finite rectangular surface where $D_x > D_y$, it can be shown numerically that the FS and BS schemes given in Fig. 3(a) and (b) require a smaller number of plane waves when the NSA algorithm is incorporated into the FB method. In addition, Tran observed that these schemes shown in Fig. 3(a) and (b) usually provide better convergence except for some types of surfaces that exhibit resonant scattering effects.

Substituting (6) into (1), (1) can be separated into two coupled integral equations

$$\boldsymbol{J}^f(\boldsymbol{r}) = \boldsymbol{J}_{PO}(\boldsymbol{r}) + 2\boldsymbol{n} \times \iint_{PV,\, S^f_{xy}} dx'\, dy' \nabla g(\boldsymbol{r}, \boldsymbol{r}') \times \left[\boldsymbol{J}^f(\boldsymbol{r}') + \boldsymbol{J}^b(\boldsymbol{r}')\right] \tag{7}$$

$$\boldsymbol{J}^b(\boldsymbol{r}) = 2\boldsymbol{n} \times \iint_{PV,\, S^b_{xy}} dx'\, dy' \nabla g(\boldsymbol{r}, \boldsymbol{r}') \times \left[\boldsymbol{J}^f(\boldsymbol{r}') + \boldsymbol{J}^b(\boldsymbol{r}')\right] \tag{8}$$

where S^f_{xy} and S^b_{xy} are the surfaces corresponding to the FS and BS processes respectively, as shown in Fig. 3(d). The adding of the results of (7) and (8) in (1), due to the fact that $S_{xy} = S^f_{xy} + S^b_{xy}$, is noted. The integral term on the right-hand side (RHS) of (7) represents the FS contribution due to the radiation of current elements belonging to the surface S^f_{xy}. Similarly, the integral term on the RHS of (8) represents the BS contribution due to the radiation of current elements belonging to the surface S^b_{xy}. (7) and (8) can be solved using an iterative method, the

FB method, by first initializing $\boldsymbol{J}^{b,(0)}(\boldsymbol{r}) = \boldsymbol{0}$, and at the kth ($k \geq 1$) iteration

$$\boldsymbol{J}^{f,(k)}(\boldsymbol{r}) = \boldsymbol{J}_{PO}(\boldsymbol{r}) + 2\boldsymbol{n} \times \iint_{PV,\, S^f{}_{xy}} dx'\, dy' \nabla g(\boldsymbol{r}, \boldsymbol{r}') \times \left[\boldsymbol{J}^{f,(k)}(\boldsymbol{r}') + \boldsymbol{J}^{b,(k-1)}(\boldsymbol{r}')\right] \tag{9}$$

$$\boldsymbol{J}^{b,(k)}(\boldsymbol{r}) = 2\boldsymbol{n} \times \iint_{PV,\, S^b_{xy}} dx'\, dy' \nabla g(\boldsymbol{r}, \boldsymbol{r}') \times \left[\boldsymbol{J}^{f,(k)}(\boldsymbol{r}') + \boldsymbol{J}^{b,(k)}(\boldsymbol{r}')\right]. \tag{10}$$

The currents $\boldsymbol{J}^{f,(k)}(\boldsymbol{r})$ in (9) are first solved for all receiving elements, and then employed in (10) to solve for the currents $\boldsymbol{J}^{b,(k)}(\boldsymbol{r})$ for all receiving elements. Iterative processes are continued in the FB fashion until surface currents exhibit convergence to within a specified accuracy criterion. The normalized pseudo-residual PR_N is used to monitor convergence of the FB method, defined as follows:

$$PR_N = \frac{\left\|\overline{I}^{(k)} - \overline{I}^{(k-1)}\right\|}{\left\|\overline{I}^{(k)}\right\|} \tag{11}$$

where $\|\cdot\|$ is the vector norm. It is noted that the PR_N convergence test does not require a matrix-vector multiply. From numerical experience in RRSS problems of interest, the convergence test based on PR_N seems to yield quite accurate results for tolerance of 0.01. However, it may not be an acceptable stopping test for general scattering problems [14].

Although the FB method provides very rapid convergence in many RRSS problems, it requires a direct computation of the matrix-vector multipliers to compute the mutual coupling between all pairs of points on the rough surface. In addition, the impedance matrix $\overline{\overline{Z}}$ must be stored at a cost of $\mathcal{O}(N_{tot}^2)$ memory storage, or all elements of the matrix must be recomputed at each iteration with a time-consuming computation.

III. Novel Spectral Acceleration Algorithm for the Forward–Backward Method (FB/NSA)

In order to accelerate the FB method mutual coupling computation, the NSA algorithm is employed to obtain $\mathcal{O}(N_{tot})$ for both CPU time and memory storage requirements. For convenience in understanding the FB/NSA method, only the computation of the FS process is considered. The BS computation can be treated in a similar fashion. The NSA algorithm starts with the selection of a neighborhood distance in the x-direction L_x, within which interactions between points are classified as strong, and outside of which, interactions are classified as weak, as illustrated in Fig. 4. It can be seen that the FS surface S^f_{xy} is decomposed into the FS strong ($S^f_{xy,\,s}$) and weak ($S^f_{xy,\,w}$) regions. Using this decomposition, (7) can be rewritten as

$$\boldsymbol{J}^{f,(k)}(\boldsymbol{r}) = \boldsymbol{J}_{PO}(\boldsymbol{r}) + \boldsymbol{J}^{f,(k)}_s(\boldsymbol{r}) + \boldsymbol{J}^{f,(k)}_w(\boldsymbol{r}) \tag{12}$$

where

$$\boldsymbol{J}^{f,(k)}_s(\boldsymbol{r}) = 2\boldsymbol{n} \times \iint_{PV,\, S^f_{xy,\,s}} dx'\, dy' G(R)\boldsymbol{R} \times \left[\boldsymbol{J}^{f,(k)}(\boldsymbol{r}') + \boldsymbol{J}^{b,(k-1)}(\boldsymbol{r}')\right] \tag{13}$$

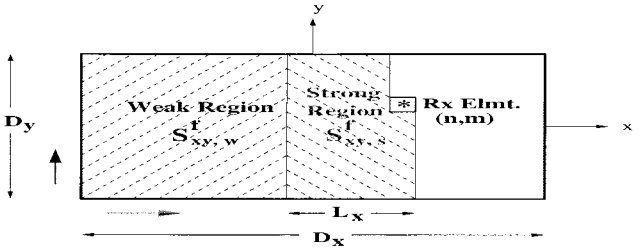

Fig. 4. Strong and weak regions in the FS direction.

$$\boldsymbol{J}^{f,(k)}_w(\boldsymbol{r}) = 2\boldsymbol{n} \times \iint_{S^f_{xy,\,w}} dx'\, dy' \nabla g(\boldsymbol{r}, \boldsymbol{r}') \times \left[\boldsymbol{J}^{f,(k)}(\boldsymbol{r}') + \boldsymbol{J}^{b,(k-1)}(\boldsymbol{r}')\right] \tag{14}$$

and $S^f_{xy} = S^f_{xy,\,s} + S^f_{xy,\,w}$. The terms $\boldsymbol{J}^{f,(k)}_s(\boldsymbol{r})$ and $\boldsymbol{J}^{f,(k)}_w(\boldsymbol{r})$ in (12) represent the strong and weak region contributions, respectively. The current $\boldsymbol{J}^{f,(k)}_s(\boldsymbol{r})$ is computed in the conventional manner, and the NSA algorithm is employed to compute the current $\boldsymbol{J}^{f,(k)}_w(\boldsymbol{r})$.

The NSA algorithm starts with the spectral representation of the free space 3-D scalar Green's function $g(\boldsymbol{r}, \boldsymbol{r}')$ for $x - x' > 0$

$$g(\boldsymbol{r}, \boldsymbol{r}') = \frac{i}{8\pi^2} \int_{C_{k_z}} \int_{C_{k_y}} dk_z\, dk_y\, \frac{e^{i\boldsymbol{k}\cdot\boldsymbol{R}}}{k_x} \tag{15}$$

where

$\boldsymbol{k}$ $= \hat{x}k_x + \hat{y}k_y + \hat{z}k_z$;
k_x $= (k^2 - k_y^2 - k_z^2)^{1/2}$;
x and x' denote the x-coordinates of a field (receiving) point and a source point, respectively [15], [16].

The contours C_{k_z} and C_{k_y} are the *original* contours of integration on the real axes in the complex k_z and k_y planes, respectively.

Applying the gradient operator ∇ to $g(\boldsymbol{r}, \boldsymbol{r}')$ in (15), the spectral representation of $\nabla g(\boldsymbol{r}, \boldsymbol{r}')$ is obtained as

$$\nabla g(\boldsymbol{r}, \boldsymbol{r}') = -\frac{1}{8\pi^2} \int_{C_{k_z}} \int_{C_{k_y}} dk_z\, dk_y\, \frac{\boldsymbol{k} e^{i\boldsymbol{k}\cdot\boldsymbol{R}}}{k_x}. \tag{16}$$

Substituting (16) into (14) and interchanging the spatial and contour integrations, (14) can be rewritten as

$$\boldsymbol{J}^{f,(k)}_w(\boldsymbol{r}) = -\frac{1}{4\pi^2}\, \boldsymbol{n} \times \int_{C_{k_z}} \int_{C_{k_y}} dk_z\, dk_y\, \frac{\boldsymbol{F}^{(k)}(\boldsymbol{r}, k_z, k_y)}{k_x} \tag{17}$$

where $\boldsymbol{F}^{(k)}(\boldsymbol{r}, k_z, k_y)$ is called the complex vector *radiation* function (or plane wave spectrum) on the kth iteration, defined as

$$\boldsymbol{F}^{(k)}(\boldsymbol{r}, k_z, k_y) = \iint_{S^f_{xy,\,w}} dx'\, dy'\, \boldsymbol{V}^{(k)}(\boldsymbol{r}') e^{i\boldsymbol{k}\cdot\boldsymbol{R}} \tag{18}$$

where

$$\boldsymbol{V}^{(k)}(\boldsymbol{r}') = \boldsymbol{k} \times \left[\boldsymbol{J}^{f,(k)}(\boldsymbol{r}') + \boldsymbol{J}^{b,(k-1)}(\boldsymbol{r}')\right].$$

Thus, weak element contributions $\boldsymbol{J}^{f,(k)}_w(\boldsymbol{r})$ can be obtained through a spectral domain integral of the complex vector radiation function $\boldsymbol{F}^{(k)}(\boldsymbol{r}, k_z, k_y)$. One property of $\boldsymbol{F}^{(k)}(\boldsymbol{r}, k_z, k_y)$

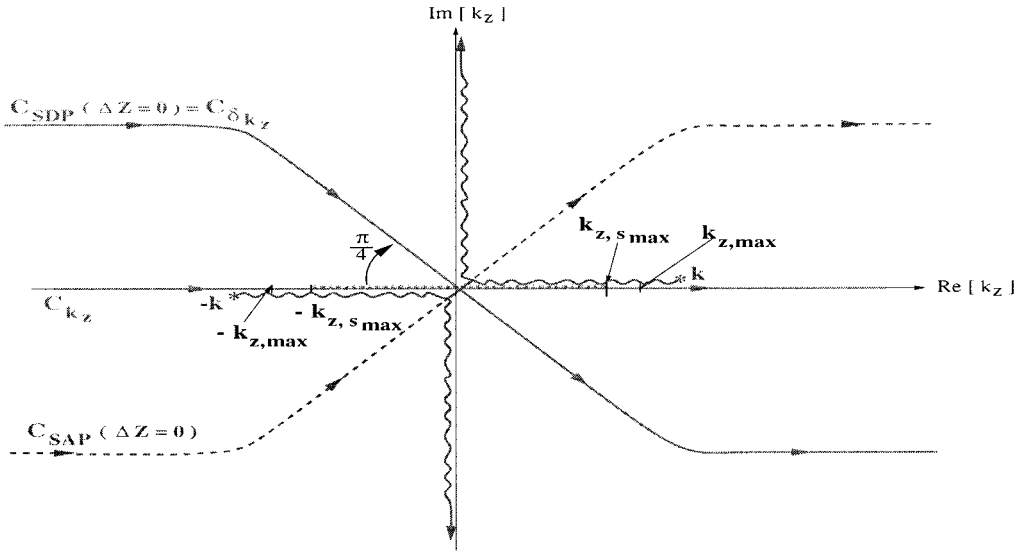

Fig. 5. Integration contour of $g(\boldsymbol{r}, \boldsymbol{r}')$ on the complex k_z plane. C_{k_z} is the original contour, and $C_{\delta_{k_z}}$ is the deformed contour. The SDP and SAP contours for a flat surface ($\Delta z = 0$) are also shown.

is that it can be computed from weak element currents in a recursive manner. To see this, let $\boldsymbol{r}_{(n,m)}$ denote a position vector starting from the origin of the coordinate system to the center of the (n, m)th element on the surface S, where $n = 1, \cdots, N$ and $m = 1, \cdots, M$. Discretizing the double spatial integral on the RHS of (18), the radiation function $\boldsymbol{F}^{(k)}(\boldsymbol{r}, k_z, k_y)$ in the FS direction can be recursively computed through a "phase shifting" process as follows:

$$\boldsymbol{F}^{(k)}(\boldsymbol{r}_{(n,m)}, k_z, k_y) = \begin{cases} \boldsymbol{F}^{(k)}\left(\boldsymbol{r}_{(n-1,M)}, k_z, k_y\right) e^{i\Psi_1} \\ \quad +\Delta S_{xy} \sum_{i=1}^{M} \boldsymbol{V}^{(k)}\left(\boldsymbol{r}_{(n-N_{L_x},i)}\right) e^{i\Psi_2}, & m = 1 \\ \boldsymbol{F}^{(k)}\left(\boldsymbol{r}_{(n,m-1)}, k_z, k_y\right) e^{i\Psi_3}, & m \neq 1 \end{cases} \tag{19}$$

where

$\Psi_1 = \boldsymbol{k} \cdot [\boldsymbol{r}_{(n,1)} - \boldsymbol{r}_{(n-1,M)}]$;
$\Psi_2 = \boldsymbol{k} \cdot [\boldsymbol{r}_{(n,1)} - \boldsymbol{r}_{(n-N_{L_x},i)}]$;
$\Psi_3 = \boldsymbol{k} \cdot [\boldsymbol{r}_{(n,m)} - \boldsymbol{r}_{(n,m-1)}]$;
$N_{L_x} = (L_x/\Delta x)$;
$\Delta S_{xy} = \Delta x \Delta y$.

(19) illustrates that the function $\boldsymbol{F}^{(k)}(\boldsymbol{r}_{(n,m)}, k_z, k_y)$ continuously updates when the receiving element is at the bottom of the 2-D grid S_{xy} ($m = 1$) as a new set of source elements enters the weak interaction group. For $m \neq 1$, the function $\boldsymbol{F}^{(k)}(\boldsymbol{r}_{(n,m)}, k_z, k_y)$ can be computed by simply multiplying the previous value $\boldsymbol{F}^{(k)}(\boldsymbol{r}_{(n,m-1)}, k_z, k_y)$ by a "phase" function.

Figs. 5–7 illustrate various contours in the complex k_z and k_y planes. A solid line indicates that a contour is in the *proper* Riemann sheet, which satisfies the radiation condition for the $e^{-i\omega t}$ harmonic time convention, while a dashed line indicates that a contour is in the *improper* Riemann sheet. To gain numerical efficiency when performing the numerical contour integration, the original contours C_{k_z} and C_{k_y} are deformed to the new contours $C_{\delta_{k_z}}$ and $C_{\delta_{k_y}}$, respectively, as shown in the above figures. This is possible since there are no singularities between the original and deformed contours. These contour deformations yield smaller integration intervals and smaller sampling rates to evaluate the double spectral integral involving $\boldsymbol{F}^{(k)}(\boldsymbol{r}, k_z, k_y)$. This is due to the fact that the function $\boldsymbol{F}^{(k)}(\boldsymbol{r}, k_z, k_y)$ is relatively smooth and localized in the complex k_z and k_y planes along the deformed complex contours, as illustrated via numerical examples later in Section V.

Advantageous deformed contours $C_{\delta_{k_z}}$ and $C_{\delta_{k_y}}$ can be determined by considering the spectral representation of $g(\boldsymbol{r}, \boldsymbol{r}')$. (15) can be rewritten as

$$g(\boldsymbol{r}, \boldsymbol{r}') = \frac{i}{8\pi^2} \int_{C_{\delta_{k_z}}} dk_z\, e^{ik_z(z-z')} \int_{C_{\delta_{k_y}}} dk_y \times \frac{e^{i\left[k_x(x-x')+k_y(y-y')\right]}}{k_x}. \tag{20}$$

It can be seen from (20) that the two spectral variables k_z and k_y are coupled through $k_x = (k^2 - k_y^2 - k_z^2)^{1/2}$. As k_z changes along the contour $C_{\delta_{k_z}}$, the topology in the complex k_y plane is modified. For convenience, first consider the topology in the complex k_z plane for a single pair of points $\boldsymbol{r}$ and $\boldsymbol{r}'$ on a flat surface. In Fig. 5, there are a pair of branch cuts originating at the branch points $\pm k$. For a flat surface, the steepest descent path (SDP) $C_{\mathrm{SDP}}(\Delta z = 0)$ and steepest ascent path (SAP) $C_{\mathrm{SAP}}(\Delta z = 0)$ intersect at the saddle point at the origin in the complex k_z plane. From an asymptotic analysis, most of the contribution occurs on portions of the SDP path near a saddle point on the real axis. As the distance from the saddle point increases along the SDP path, the integrand of (20) with respect to k_z is exponentially attenuated so that the contributions become negligible. Thus, it is numerically advantageous to deform the original contour C_{k_z} to the SDP contour for a flat surface $C_{\mathrm{SDP}}(\Delta z = 0)$.

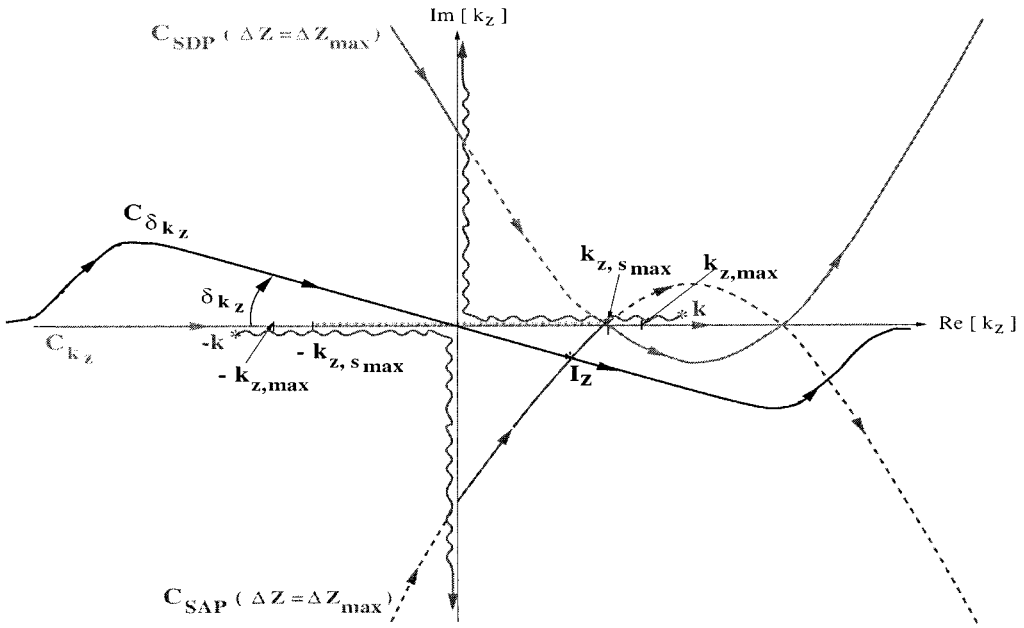

Fig. 6. Integration contour of $g(\boldsymbol{r}, \boldsymbol{r}')$ on the complex k_z plane. $C_{\rm SDP}(\Delta z = \Delta z_{\rm max})$ and $C_{\rm SAP}(\Delta z = \Delta z_{\rm max})$ are the SDP and SAP contours when $\Delta z = \Delta z_{\rm max}$ respectively.

An SDP path can also be determined for a pair of points $\boldsymbol{r}$ and $\boldsymbol{r}'$ with $\Delta z = |z - z'| \neq 0$, for which the saddle point is located at

$$k_{z,\,s} = \frac{k(z - z')}{\sqrt{|\boldsymbol{\rho} - \boldsymbol{\rho}'|^2 + (z - z')^2}} \tag{21}$$

where $\boldsymbol{\rho} = \hat{x}x + \hat{y}y$ and $\boldsymbol{\rho}' = \hat{x}x' + \hat{y}y'$, as illustrated in Fig. 6, but the path equation is more complicated. However, when coupling between many pairs of points is considered as in the weak region contribution to the (n, m)th receiving element, there is no longer a unique SDP path for a rough surface along which only attenuation of the integrand is obtained away from a single saddle point. Thus, the deformed contour $C_{\delta_{k_z}}$ must be chosen as a compromise between extreme exponential growth and rapid oscillation of the integrand. Let $\Delta z_{\rm max}$ denote the largest surface variation, which is equal to $z_{\rm max} - z_{\rm min}$. The saddle points in this case are distributed along the real axis between $\pm k_{z,\,s_{\rm max}}$, where $k_{z,\,s_{\rm max}}$ is the outermost possible saddle point on the real axis when $\Delta z = \Delta z_{\rm max}$ and $|\boldsymbol{\rho} - \boldsymbol{\rho}'| = L_x$. Consider contours $C_{\rm SDP}(\Delta z = \Delta z_{\rm max})$ and $C_{\rm SAP}(\Delta z = \Delta z_{\rm max})$, which intersect at the saddle point $k_{z,\,s_{\rm max}}$, computed numerically in Fig. 6. It is noted that the portion of the deformed contour $C_{\delta_{k_z}}$ between $\pm k_{z,\,s_{\rm max}}$ mixes both descent and ascent paths where the integrand of (20) with respect to k_z may exponentially increase. Note that the magnitude of the integrand is maximum near the intersection point I_z, as shown in Fig. 6, where the SAP contour $C_{\rm SAP}(\Delta z = \Delta z_{\rm max})$ intersects the deformed contour $C_{\delta_{k_z}}$. For convenience, when performing the numerical integration, the contour $C_{\delta_{k_z}}$ is defined to be a straight line, making an angle δ_{k_z} with respect to the negative real axis in the interval from $-k_{z,\,\rm max}$ to $k_{z,\,\rm max}$, where $k_{z,\,\rm max}$ is the upper limit of integration that will be specified later. Outside this interval, the contour $C_{\delta_{k_z}}$ is deformed and joined to the original contour C_{k_z} (the real axis). It is noted that the contribution of the integral along $C_{\delta_{k_z}}$ outside the interval is negligible due to either exponential attenuation or fast oscillation of the integrand. For a flat surface, δ_{k_z} is chosen to be $\pi/4$, which is the angle of $C_{\rm SDP}(\Delta z = 0)$ measured with respect to the negative real axis. For a rough surface, δ_{k_z} must be chosen to be smaller than or equal to $\pi/4$ to avoid extreme growth rates in the interval from $-k_{z,\,s_{\rm max}}$ to $k_{z,\,s_{\rm max}}$, where the contour $C_{\delta_{k_z}}$ mixes both descent and ascent paths.

Numerical tests show that $\delta_{k_z} = \pi 4$ still provides accurate results when $\tan^{-1}(\Delta z_{\rm max}/L_x) \leq 0.1$. However, when $\tan^{-1}(\Delta z_{\rm max}/L_x) > 0.1$, δ_{k_z} can be obtained by limiting the maximum of the integrand on the contour $C_{\delta_{k_z}}$ to $e^{a_{\rm max}}$, where $a_{\rm max}$ is some constant to be determined later. Based on numerical experiments, $a_{\rm max}$ is typically found to be less than three. Employing this criterion and performing a first-order Taylor's series expansion of the SAP contour $C_{\rm SAP}(\Delta z = \Delta z_{\rm max})$ in the neighborhood of the saddle point $k_{z,\,s_{\rm max}}$ results in a nonlinear equation, which must be solved to determine δ_{k_z}. A two-step procedure is involved. First, numerically solving the following nonlinear equation for ξ, where ξ is a possible value of $1/\tan\delta_{k_z}$

$$L_x\sqrt{\tau_1 - \tau_2} + \tau_3 = 0 \tag{22}$$

where

$$\begin{aligned}
\tau_1 &= 0.5\sqrt{4\tau_2^2 + \tau_4^2};\\
\tau_2 &= 0.5[k^2(1+\xi)^2 + k_{z,\,s_{\rm max}}^2(1-\xi^2)];\\
\tau_3 &= (1+\xi)a_{\rm max} - k_{z,\,s_{\rm max}}\Delta z_{\rm max};\\
\tau_4 &= 2\xi k_{z,\,s_{\rm max}}^2.
\end{aligned}$$

Once ξ is solved, δ_{k_z} can be determined as follows

$$\delta_{k_z} = \tan^{-1}\left[\frac{1}{\max\{\xi,\,1\}}\right], \quad \tan^{-1}\left(\frac{\Delta z_{max}}{L_x}\right) > 0.1. \tag{23}$$

Next, consider the topology in the complex k_y plane, which varies with k_z as illustrated in (20). Note also that surface roughness is not involved in (20) but the y-dimension of the surface

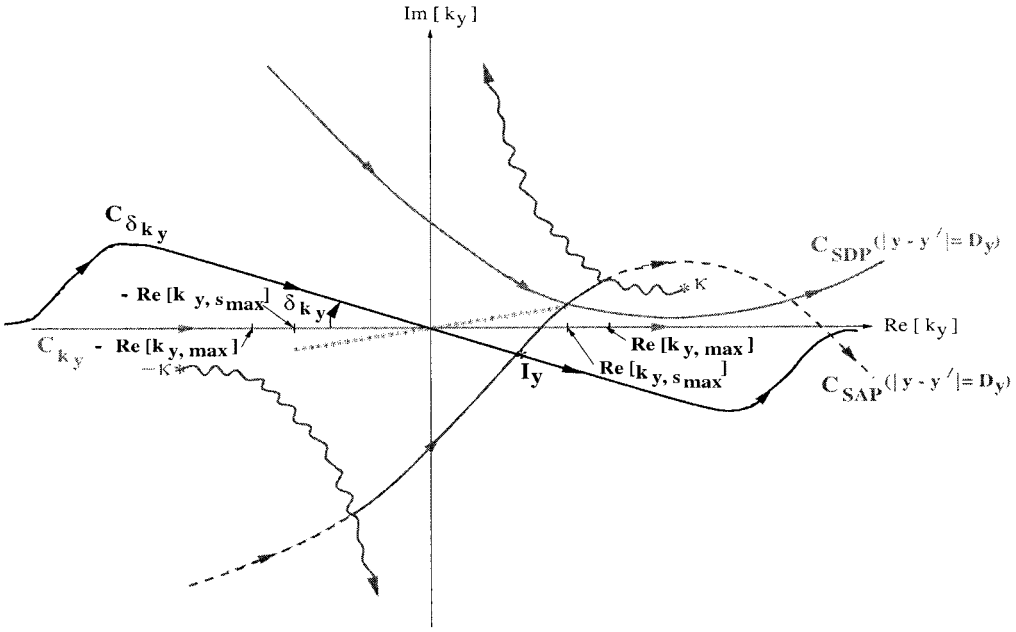

Fig. 7. Integration contour of $g(\boldsymbol{r}, \boldsymbol{r}')$ on the complex k_y plane for a fixed value of k_z. C_{k_y} is the original contour, and $C_{\delta_{k_y}}$ is the deformed contour.

D_y appears as a "roughness" parameter. For a fixed value of k_z, the topology in the complex k_y plane is illustrated in Fig. 7. A pair of branch cuts originating from the branch points $\pm\kappa$, where $\kappa = (k^2 - k_z^2)^{1/2} = \kappa' + i\kappa''$, are observed in Fig. 7 with κ' and κ'' defined to be greater than or equal to 0. It is noted that κ acts as a complex propagation constant in the k_y plane. In general, an SDP path can be determined from a pair of points $\boldsymbol{r}$ and $\boldsymbol{r}'$ with the saddle point located at

$$k_{y,\,s} = \frac{\kappa(y - y')}{|\boldsymbol{\rho} - \boldsymbol{\rho}'|}. \tag{24}$$

Like the analysis in the complex k_z plane, there is no unique SDP path for the rough surface case. The saddle points in this case are distributed along the straight line joining the branch points $\pm\kappa$. The saddle point real coordinate ranges from $-\mathrm{Re}[k_{y,\,s_{\max}}]$ to $\mathrm{Re}[k_{y,\,s_{\max}}]$, where $k_{y,\,s_{\max}}$ is the outermost saddle point on the above line when $y - y' = D_y$ and $|\boldsymbol{\rho} - \boldsymbol{\rho}'| = \sqrt{L_x^2 + D_y^2}$, and Re[·] denotes the real part of its argument. The contours $C_{\mathrm{SDP}}(y - y' = D_y)$ and $C_{\mathrm{SAP}}(y - y' = D_y)$ intersect at the saddle point $k_{y,\,s_{\max}}$. Let $\mathrm{Re}[k_{y,\,\max}]$ denote the upper limit of the integration on the real axis, which is specified later. In the interval between $-\mathrm{Re}[k_{y,\,\max}]$ and $\mathrm{Re}[k_{y,\,\max}]$, the deformed contour $C_{\delta_{k_y}}$ is a straight line with the slope $-\tan(\delta_{k_y})$. Outside this interval, the contour $C_{\delta_{k_y}}$ is deformed and joined to the original contour C_{k_y}. As in the case of the angle δ_{k_z}, it can be shown numerically that $\delta_{k_y} = \pi/4$ provides accurate results when $\tan^{-1}(D_y/L_x) \leq 0.1$. However, when $\tan^{-1}(D_y/L_x) > 0.1$, it is quite difficult to obtain an analytical formula for δ_{k_y} due to the complexity of the topology in the complex k_y plane. For convenience in discussion later, let $\gamma (0 < \gamma \leq \pi/4)$ be the value of δ_{k_y} for this case. One solution to this problem is to determine δ_{k_y} empirically by comparing the analytical solution of $g(\boldsymbol{r}, \boldsymbol{r}')$ to the solution obtained from its spectral domain representation. This empirical procedure of determining γ for a given finite surface size, surface statistics, and L_x will be explained in more detail later. Note that the appearance of D_y as a roughness parameter makes the method most suited for rectangular surfaces with large D_x/D_y ratios.

Once the deformed contours $C_{\delta_{k_z}}$ and $C_{\delta_{k_y}}$ are known, (17) can be rewritten in terms of $C_{\delta_{k_z}}$ and $C_{\delta_{k_y}}$ as

$$\boldsymbol{J}_w^{f,\,(k)}(\boldsymbol{r}) = -\frac{1}{4\pi^2}\,\boldsymbol{n} \times \int_{C_{\delta_{k_z}}} \int_{C_{\delta_{k_y}}} dk_z\, dk_y \frac{\boldsymbol{F}^{(k)}(\boldsymbol{r},\, k_z,\, k_y)}{k_x}. \tag{25}$$

For convenience when performing the numerical double contour integration, the double contour integral of (25) is discretized and mapped to the real axis according to the following mappings: $dk_z \rightarrow \Delta k_z e^{-i\delta_{k_z}}$, $k_z \rightarrow k_{z_p} = p\Delta k_z e^{-i\delta_{k_z}}$ for $p = -P, \cdots, P$, $dk_y \rightarrow \Delta k_y e^{-i\delta_{k_y}}$, and $k_y \rightarrow k_{y_q} = q\Delta k_y e^{-i\delta_{k_y}}$ for $q = -Q_p, \cdots, Q_p$, where Δk_z and Δk_y are the integration step sizes in the complex k_z and k_y planes, respectively, and $2P+1$ is the number of plane waves in the k_z plane. It is noted that Q_p depends on p, and it can be shown that $Q_{-p} = Q_p$. Thus, for a fixed k_z (p is fixed), the number of plane waves in the k_y plane is equal to $2Q_p + 1$ and the total number of plane waves in both planes Q_{TOT} is given by

$$Q_{\mathrm{TOT}} = \sum_{p=-P}^{P} (2Q_p + 1) \tag{26}$$

where $P = (k_{z,\,\max}/\Delta k_z) + 1$ and $Q_p = (\mathrm{Re}[k_{y,\,\max}]/\Delta k_y) + 1$. Using the above mapping, the discretized version of (25) can be written as

$$\boldsymbol{J}_w^{f,\,(k)}(\boldsymbol{r}) = -\frac{1}{4\pi^2}\Delta\Omega \sum_{p=-P}^{P} \sum_{q=-Q_p}^{Q_p} \times \frac{W(k_{z_p},\, k_{y_q}) \left[\boldsymbol{n} \times \boldsymbol{F}^{(k)}(\boldsymbol{r},\, k_{z_p},\, k_{y_q})\right]}{k_{x_{p,\,q}}} \times e^{-i\delta_{k_z}} e^{-i\delta_{k_y}} \tag{27}$$

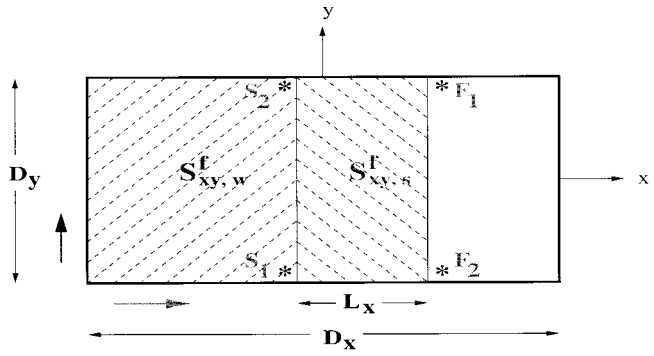

Fig. 8. Worst-case configuration of a pair of source and field points for computing $g(\boldsymbol{r}, \boldsymbol{r}')$.

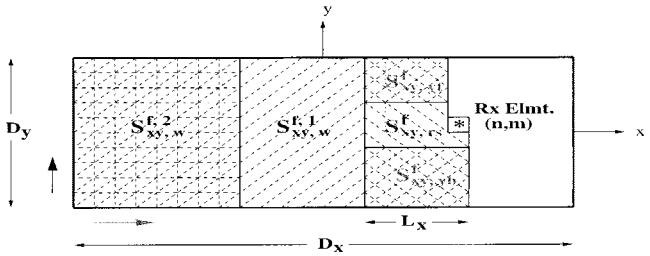

Fig. 9. Decomposition of regions in the FS direction for extremely large-scale 2-D RRSS problems.

where

$k_{x_{p,q}} = (k^2 - k_{y_q}^2 - k_{z_p}^2)^{1/2}$;
$\Delta\Omega = \Delta k_y \Delta k_z$;
$W(k_{z_p}, k_{y_q})$ weighting function for numerical integration.

Various integration parameters in the k_z and k_y planes are given as follows:

$$k_{z,\max} = \begin{cases} \sqrt{\dfrac{20k}{L_x}}, & \tan^{-1}\left(\dfrac{\Delta z_{\max}}{L_x}\right) \le 0.1 \\ k_{z,s_{\max}} & \\ \quad +k_{z,tail}, & \tan^{-1}\left(\dfrac{\Delta z_{\max}}{L_x}\right) > 0.1 \end{cases} \tag{28}$$

$$\mathrm{Re}[k_{y,\max}] = \begin{cases} \sqrt{\dfrac{20k}{L_x}}, & \tan^{-1}\left(\dfrac{D_y}{L_x}\right) \le 0.1 \\ \mathrm{Re}[k_{y,s_{\max}}] & \\ \quad +k_{y,tail}, & \tan^{-1}\left(\dfrac{D_y}{L_x}\right) > 0.1, \end{cases} \tag{29}$$

and $k_{z,s_{\max}} = (k\Delta z_{\max}/R_{xz})$, $\Delta k_z = (1/22)\sqrt{(C_z k/L_x)}$, $k_{y,s_{\max}} = (\kappa D_y/R_{xy})$, and $\Delta k_y = (1/22)\sqrt{(C_y k/R_{xy})}$, where $R_{xz} = \sqrt{L_x^2 + (\Delta z_{\max})^2}$ and $R_{xy} = \sqrt{L_x^2 + D_y^2}$. The constants $k_{z,tail}$, $k_{y,tail}$, C_z, and C_y are to be determined. The first lines of (28) and (29) and the forms for Δk_z and Δk_y are obtained by studying the behavior of the integrand of (15) for the flat surface case and employing the physical optics approximation for the current distribution on the rough surface, and numerical tests confirm the accuracy of these expressions. It is noted that the constants $k_{z,tail}$ and $k_{y,tail}$ are some tolerances added to $k_{z,s_{\max}}$ and $k_{y,s_{\max}}$, respectively, to ensure that the integrand of (15) is exponentially decayed. Note that increasing C_z and C_y results in a smaller number of plane waves required, while increasing $k_{z,tail}$ and $k_{y,tail}$ results in a larger number of plane waves.

One way to determine the unknown constants γ, $a_{\max}$, $k_{z,tail}$, $k_{y,tail}$, C_z, and C_y for large-scale surfaces is to study the scalar Green's function $g(\boldsymbol{r}, \boldsymbol{r}')$ for a pair of source and field points in the worst-case scenario for computing $g(\boldsymbol{r}, \boldsymbol{r}')$ in the spectral domain. Comparing the exact solution of $g(\boldsymbol{r}, \boldsymbol{r}')$ to its spectral domain solution within a specified accuracy, these unknown constants can be determined. For convenience, consider only the FS direction. Fig. 8 illustrates this worst-case configuration of a pair of source and field points. In this figure, S_i and F_i denote source and field points, respectively, where i =1, 2. In the spectral domain point of view, this configuration of source and field points (S_1 and F_1 or S_2 and F_2) yields the outermost saddle point $k_{y,s_{\max}}$ in the k_y plane. The SAP path $C_{\mathrm{SAP}}(y - y' = D_y)$ passes through $k_{y,s_{\max}}$ and intersects the deformed contour $C_{\delta_{k_y}}$ at I_y, where the integrand is nearly maximum, as shown in Fig. 7. In addition, $k_{z,s}$ in this configuration is close to $k_{z,s_{\max}}$, since $x - x'$ is minimum ($x - x' = L_x$ and assuming that $\Delta z \to \Delta z_{\max}$). Other source points in the region $S^f_{xy,w}$ yield $-k_{z,s_{\max}} < k_{z,s} < k_{z,s_{\max}}$ and $-\mathrm{Re}[k_{y,s_{\max}}] < Re[k_{y,s}] < \mathrm{Re}[k_{y,s_{\max}}]$. It should be pointed out that the unknown constant $k_{z,tail}$ can be determined first by considering the case when the source and field points are located at the same y-coordinate (e.g., S_1 and F_2 or S_2 and F_1). This is due to the fact that the difference $y - y'$ does not directly influence the exponentially decayed behavior of the integrand with respect to k_z in the interval outside $\pm k_{z,s_{\max}}$. Numerical values of these constants for specific examples are provided in Sections IV and V.

It is noted that the integration parameters given in this section (for large-scale surfaces) may not yield accurate results for a pair of points $\boldsymbol{r}$ and $\boldsymbol{r}'$, where $x - x' \gg L_x$ corresponding to *extremely* large-scale surfaces, since they are determined by considering the worst-case configuration only (i.e., separated by $x - x' = L_x$). One way to solve this problem is to decompose the old weak region $S^f_{xy,w}$ into more than one weak regions, as illustrated in Fig. 9 for the FS direction. Appropriate integration parameters are then determined for each separate region. In addition, extremely large-scale rough surfaces with large D_y require a large approximate strong region of size $L_x \times D_y$ or a significant increase in the total number of plane waves Q_{TOT}. To reduce the size of the strong region $S^f_{xy,s}$, the old $L_x \times D_y$ approximate strong region can be decomposed into three separate regions, as also shown in Fig. 9. The surface $S^f_{xy,rs}$ is the reduced strong region. The surfaces $S^f_{xy,yt}$ and $S^f_{xy,yb}$ are the weak regions that employ the spectral domain expansion in the y-direction for $y < y'$ and $y > y'$, respectively. These decompositions can be advantageous when considering extremely large-scale 2-D rough surfaces and are still under investigation. In the next section, the computational cost and memory storage requirements of the FB/NSA method for 2-D RRSS problems are discussed.

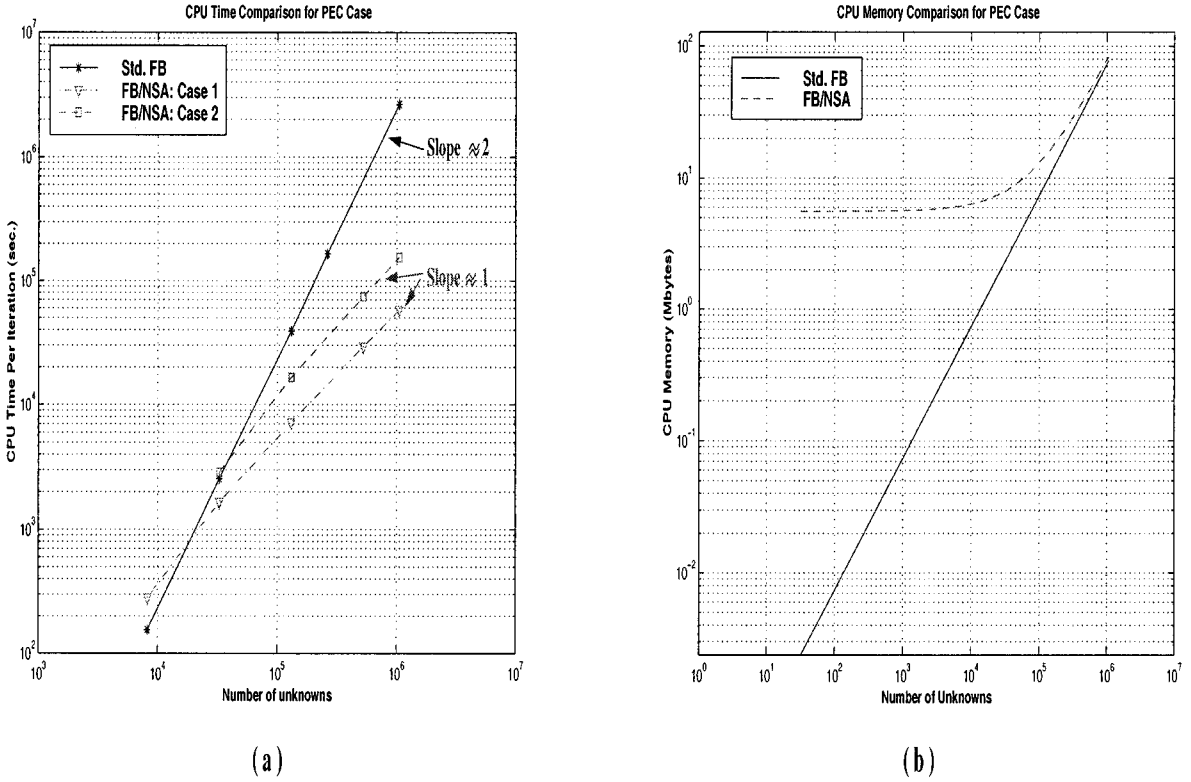

Fig. 10. Comparison of computational efficiency between the conventional FB and FB/NSA methods for 2-D PEC RRSS problems. (a) CPU time per iteration versus number of unknowns. (b) CPU memory versus number of unknowns.

IV. Computational Cost and Memory Storage Requirement of the FB/NSA Method

The total operational count (TOC) of the FB/NSA method to compute the strong-region contribution using direct matrix-vector multiply, and the weak-region contribution with the NSA algorithm [see (19) and (27)] is estimated as follows:

$$\text{TOC} \sim C_s N_s N_{elmt} + C_w Q_{\text{TOT}}(N_{elmt} - N_s) \tag{30}$$

where $N_{elmt} = NM = 0.5N_{tot}$, $N_s = N_{L_x} M$, and C_i are constants. It is noted that N_{elmt} is the total number of elements on the surface S_{xy}, and N_s is approximately the total number of elements in the strong region. The first term on the RHS of (30) is the number of operations involved in the computation of the strong-region contribution for N_{elmt} receiving elements, and the second term involves the number of operation count to compute Q_{TOT} plane waves in (27) for $N_{elmt} - N_s$ source elements in the weak region. In addition, the total memory storage requirement (TMSR) of the FB/NSA method is estimated as follows:

$$\text{TMSR} \sim C_v N_{elmt} + C_Q Q_{\text{TOT}} \tag{31}$$

where C_i are some constants. The first term on the RHS of (31) accounts for the storage of necessary matrices and vectors used in the FB/NSA method, and the second term involves the storage of the total number of plane waves. It is noted from (31) that there is no storage for matrix elements associated with the strong region since they are recalculated on each FB iteration to reduce overall memory storage.

Numerical tests show that the neighborhood distance L_x is dependent on D_y. As D_y increases, L_x should be increased to compromise between the total number of plane waves used in the FB/NSA algorithm and the size of $L_x \times D_y$. However, for fixed D_y, frequency, and surface roughness, the parameters L_x, N_s and Q_{TOT} are fixed, and as D_x increases, it can be seen from (30) and (31) that TOC and TMSR are $\mathcal{O}(N_{tot})$. Thus, the FB/NSA method is an extremely efficient method for studying low grazing-angle RRSS problems in which $D_x \gg D_y$.

Fig. 10(a) and (b) illustrates plots of CPU time per iteration and CPU memory versus number of unknowns respectively, based on a Pentium II 200 MHz computer with 128 Mb of RAM. Due to the D_y-dependency of the FB/NSA method, two surface sizes of different D_y are considered. Surfaces sizes of interest are scaled in terms of the electromagnetic wavelength λ and sampled with eight points per λ. Case 1 has $D_x(\lambda) \times 8\lambda$ Gaussian surfaces with a Gaussian spectrum given by

$$W(k_x, k_y) = \frac{l_x l_y h^2}{4\pi} e^{-(1/4)(k_x^2 l_x^2 + k_y^2 l_y^2)} \tag{32}$$

where

- $W(k_x, k_y)$ spectrum amplitude in m^4;
- l_x and l_y correlation lengths in the x- and y- directions, respectively;
- h surface root mean square (RMS) height;
- k_x and k_y spatial frequencies in the x- and y-directions, respectively.

The maximum value of D_x considered is equal to 1024 λ, resulting in 1 048 576 unknowns. In this case, the surface spectrum parameters are $h = 0.5\lambda$ and $l_x = l_y = 1.414\lambda$. In addition,

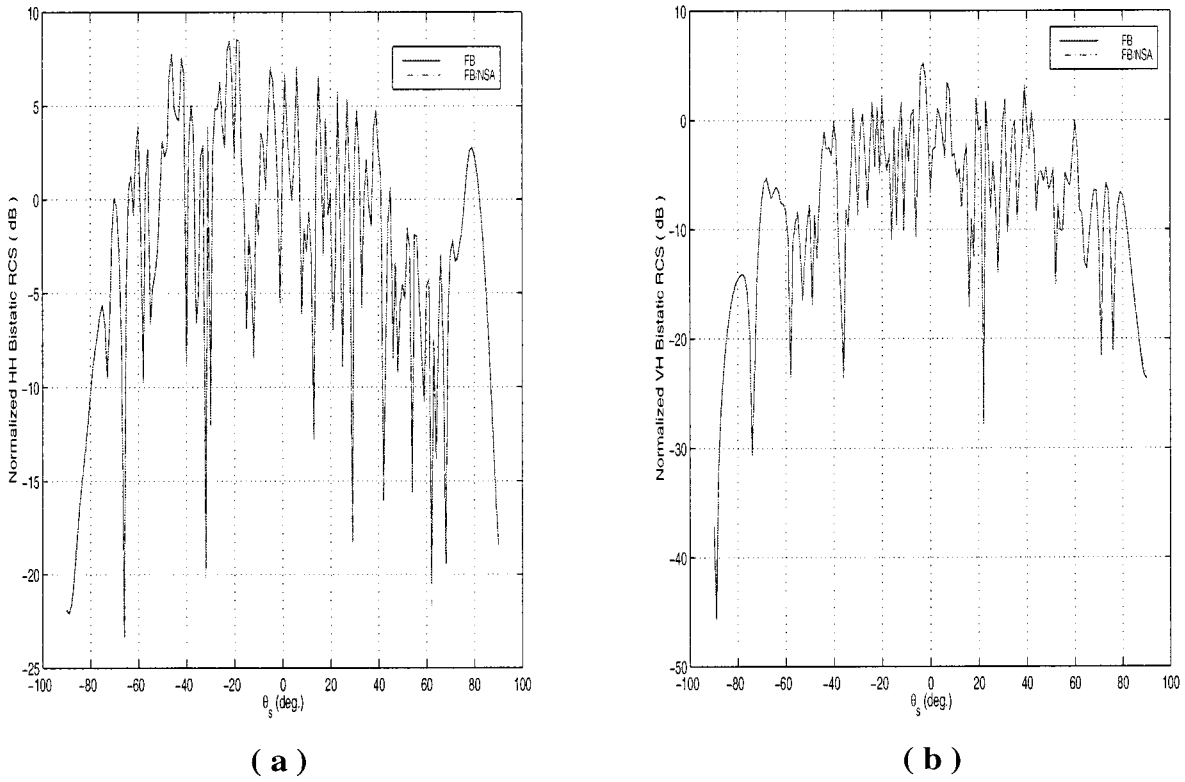

Fig. 11. Normalized bistatic RCS in dB. (a) HH polarization and (b) VH polarization.

the FB/NSA method employs the following parameters to obtain 1% accuracy in the scalar Green's function for $x - x' = L_x$: $L_x = 3.5\lambda$, $a_{\max} = 1.0$, $\delta_{k_y} = 0.1$, $k_{z,tail} = 0.35k$, $k_{y,tail} = 0.25\,\mathrm{Re}[\kappa]$, $C_z = 30.0$, and $C_y = 11.0$. Another case, Case 2, involves $D_x(\lambda) \times 32\lambda$ Gaussian surfaces with a power law spectrum given by

$$W(k,\,\phi) = a_0 k^{-4}, \quad k_{dl} < k < k_{du} \tag{33}$$

where $W(k,\,\phi)$ represents the spectrum amplitude, k denotes the spatial wave number of the surface, ϕ represents the azimuthal angle of the 2-D spectrum, a_0 is a specified constant, and k_{dl} and k_{du} are the lower and upper cutoff spatial wave numbers, respectively. The maximum value of D_x considered is equal to 256 λ, resulting in 1 048 576 unknowns. In this case, the surface spectrum parameters are $a_0 = 0.6365\times10^{-3}$, $k_{dl} = 4.5\,m^{-1}$, and $k_{du} = 587.0\,m^{-1}$. Furthermore, the FB/NSA method employs the following parameters to obtain 1% accuracy: $L_x = 3.0\lambda$, $a_{\max} = 1.0$, $\delta_{k_y} = 0.03$, $k_{z,tail} = 0.45k$, $k_{y,tail} = 0.20\,\mathrm{Re}[\kappa]$, $C_z = 25.0$, and $C_y = 11.0$.

Fig. 10(a) illustrates a comparison of CPU time per iteration (in seconds) between the conventional FB method and the FB/NSA method versus the number of unknowns for two cases on a log–log scale. It is noted that the CPU time per iteration of the standard FB method is independent of D_y. Thus, both Case 1 and 2 provide the same CPU time. In the log–log scale, the plot of CPU time versus number of unknowns is found to be a straight line for a large number of unknowns. The plot of the conventional FB method has a slope approximately equal to two, while the FB/NSA method has a slope approximately equal to one for both cases. However, the CPU time of the FB/NSA method for Case 2 is greater than for Case 1. This is due to the fact that the size of the strong region in Case 2 ($3\lambda \times 32\lambda$) is greater than in Case 1 ($3.5\lambda \times 8\lambda$), and Case 2 requires a larger number of plane waves Q_{TOT} in the NSA algorithm than Case 1. Fig. 10(b) shows a comparison of the CPU memory (Mb) versus number of unknowns between the conventional FB and FB/NSA methods. For convenience, it is assumed that the maximum number of plane waves $Q_{TOT,\max}$ is equal to 10^5. This is sufficient for both cases to provide accurate results. As the number of unknowns increases, the memory requirements of the FB/NSA method approach those of the FB method. From the plot, large-scale surfaces with 1 048 576 unknowns require a CPU memory of approximately 100 Mb, a remarkably low memory storage requirement compared to other fast algorithms. Thus, it can be concluded from these plots that the NSA algorithm can yield a great reduction in CPU time for very large problems while only slightly increasing the memory storage requirement. In the next section, several numerical results are illustrated.

V. Results and Discussions

To illustrate the computational efficiency and accuracy of the NSA algorithm, consider a deterministic $128\lambda \times 8\lambda$ PEC rough surface illuminated by a tapered plane wave with the tapered parameter $g' = 6$ [13] at an incident angle of 20°. The surface is a realization of a Gaussian random process described by a Gaussian spectrum with $l_x = l_y = 1.414\lambda$ and $h = 0.5\lambda$ having $z_{\min} = -1.888\lambda$ and $z_{\max} = 2.098\lambda$. The surface is sampled

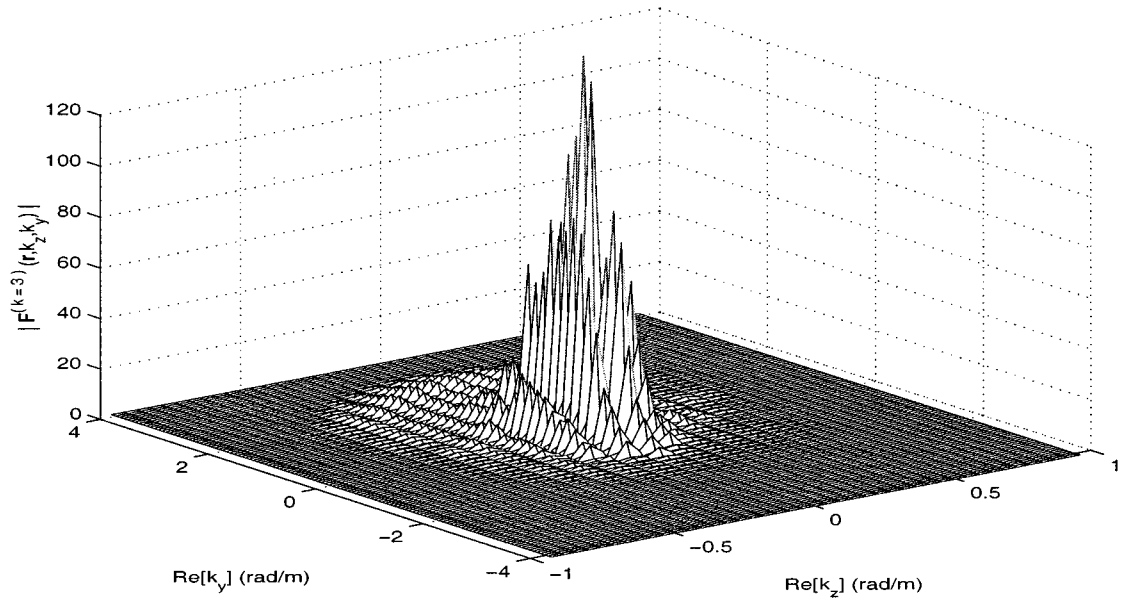

Fig. 12. Radiation function $\boldsymbol{F}^{(k)}(\boldsymbol{r}, k_z, k_y)$ in the complex k_z and k_y planes for the last backward sweep ($k = 3$) and the receiving element located at the (x_1, y_1) element of the rough surface.

with eight points per λ resulting in 131 072 unknowns for x- and y-polarization surface currents. The standard FB method is employed to compare with the FB/NSA method and requires three iterations to converge to within 1% accuracy based on the PR_N test. Its total CPU time for this example is 1976.2 min. The FB/NSA method employs the parameters of Case 1 and requires the same number of iterations to converge within the same accuracy as in the FB method. However, its total CPU time is 359.8 min. Thus, with the NSA algorithm, a CPU time reduction of 5.5 is achieved in this case.

Numerical results are presented in terms of the normalized bistatic radar cross section (RCS) $\sigma_{\alpha\beta}(\theta_s, \phi_s)$, defined for a scattered wave in α-polarization and an incident wave in β-polarization as

$$\sigma_{\alpha\beta}(\theta_s, \phi_s) = \lim_{r\to\infty} \frac{4\pi r^2 |\boldsymbol{E}^s_\alpha|^2 \cos\theta_i}{2\eta \int_S \boldsymbol{S}^i_\beta \cdot \hat{n}\, ds} \tag{34}$$

where $\boldsymbol{E}^s_\alpha$ is the α-polarized scattered field, η is the free space intrinsic impedance, $\hat{n} = \boldsymbol{n}|\boldsymbol{n}|$ is a unit normal vector pointing out of the rough surface into the free space region, and $\boldsymbol{S}^i_\beta$ is the time average Poynting vector of the β-polarized incident wave. Fig. 11(a) and (b) illustrates plots of the normalized bistatic RCS in dB when $\phi_i = \phi_s = 0^\circ$ (in plane scattering) versus the scattering angle (θ_s) for HH- and VH-polarizations, respectively, comparing between the standard FB and FB/NSA methods. From the plots, the normalized bistatic RCS obtained from both methods are in good agreement. In addition, it is also found that the average relative error of the magnitude of surface currents in the main beam is about 0.1%. Thus, the FB/NSA method provides very accurate results with a great reduction of CPU time, which stems from the properties of the complex vector radiation function $\boldsymbol{F}^{(k)}(\boldsymbol{r}, k_z, k_y)$, which can be computed recursively via (19). $\boldsymbol{F}^{(k)}(\boldsymbol{r}, k_z, k_y)$ is also relatively smooth (compared to the function obtained from integrating along the original contours) and localized in the complex k_z and k_y planes as illustrated in Fig. 12. In this figure, the magnitude of $\boldsymbol{F}^{(k)}(\boldsymbol{r}, k_z, k_y)$ of the above example is plotted versus Re$[k_z]$ and Re$[k_y]$ for the last backward sweep $k = 3$ with the receiving element located at the (x_1, y_1) element of the rough surface. The plot $\boldsymbol{F}^{(k=3)}(\boldsymbol{r}, k_z, k_y)$ is indeed localized and relatively smooth in the complex planes as a result of contour deformation from the real axis.

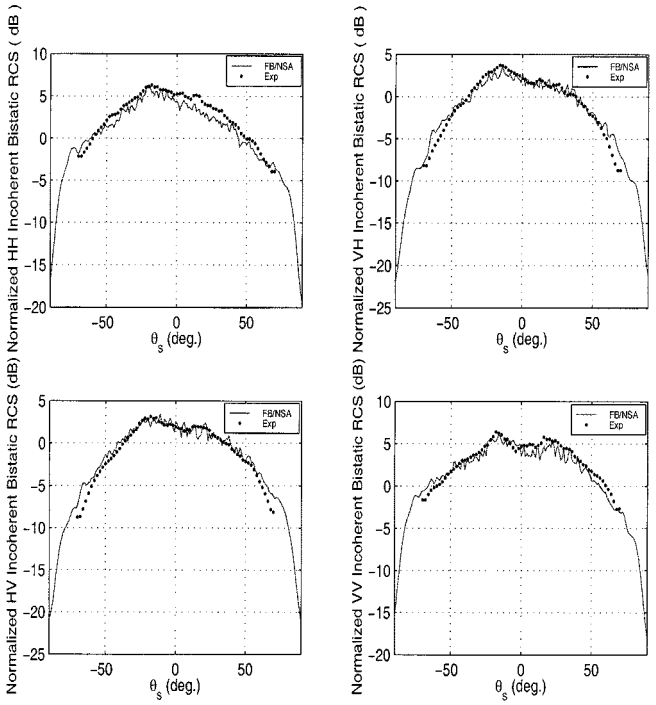

Fig. 13. Comparison between Monte Carlo simulation results computed via the FB/NSA method and the experimental data for moderately rough surfaces.

Another example illustrates the application of the FB/NSA method for moderately rough surfaces to study the backscattering enhancement phenomenon. In this example, the rough surface statistics and the tapered parameters of the incident beam are the same as in the first example, except h is increased from 0.5λ to 1.0λ in order to see the backscattering enhancement phenomenon more clearly. The FB/NSA method is employed to perform the Monte Carlo simulation numerically for 100 realizations. The following FB/NSA parameters are used: $L_x = 4.5\lambda$, $a_{\max} = 1.0$, $\delta_{k_y} = 0.1$, $k_{z,tail} = 0.15k$, $k_{y,tail} = 0.20\ \mathrm{Re}[\kappa]$, $C_z = 10.0$, and $C_y = 20.0$. Fig. 13 shows the plots of the normalized bistatic RCS versus the scattering angle θ_s for both copolarizations (HH and VV) and cross-polarizations (VH and HV). Results are compared with experimental data obtained from the University of Washington, Seattle, WA [13]. The backscattering enhancement phenomenon can be observed at $\theta_s = -20^\circ$, corresponding to the backscattering direction of an incident angle of 20° used in this simulation. In addition, Monte Carlo simulations based on the FB/NSA method are shown to reproduce the overall trends and level of the experimental data. Minor differences between the numerical and experimental Monte Carlo simulations may come from the differences between the numerical and experimental antenna patterns and the rough surface profiles that were fabricated for the experiment, as described in [13].

VI. Conclusions

The FB/NSA method has been shown to be a very efficient method for 1-D, moderately rough surfaces. In this paper, it is extended to treat 2-D large-scale PEC random rough surfaces. The new NSA algorithm for the 2-D case is derived and involves a double spectral integral representation of source currents and the 3-D free space scalar Green's function $g(\boldsymbol{r}, \boldsymbol{r}')$. The coupling between two spectral variables is complex, and the method is most suited for rectangular surfaces due to the treatment of surface cross-range size as a "roughness" parameter. The NSA parameters for this case can be obtained by comparing the exact and spectral domain representation solutions of $g(\boldsymbol{r}, \boldsymbol{r}')$ for the worst-case configuration of the source and field points, as shown in Fig. 8.

The computational efficiency of the FB/NSA method for 2-D RRSS problems is shown to be $\mathcal{O}(N_{tot})$ for fixed D_y, frequency, and surface roughness. The memory storage requirement of the method is remarkably low, resulting in larger surface sizes that can be run on present computers. In addition, the FB/NSA method still remains very efficient for moderately rough surfaces. Comparisons of numerical results between the standard FB and FB/NSA methods have shown that the FB/NSA method yields very accurate results with a great reduction of CPU time and only slightly larger memory storage requirements. Thus, it is a good candidate for studying the physics of moderately rough surface scattering at low grazing angles. Monte Carlo simulations for this case will be considered in future studies.

References

[1] H.-T. Chou and J. T. Johnson, "A novel acceleration algorithm for the computation of scattering from rough surfaces with the forward-backward method," *Radio Sci.*, vol. 33, pp. 1277–1287, 1998.

[2] R. F. Harrington, *Field Computation by Moment Methods*. Malabar, FL: Krieger, 1982.

[3] J. J. H. Wang, *Generalized Moment Methods in Electromagnetics*. New York: Wiley, 1991.

[4] E. K. Miller, L. Medgyesi-Mitschang, and E. H. Newman, *Computational Electromagnetics—Frequency-Domain Method of Moments*. New York: IEEE Press, 1992.

[5] D. Holliday, L. L. Deraad, and G. J. St-Cyr, "Forward-backward: A new method for computing low-grazing angle scattering," *IEEE Trans. Antennas Propagat.*, vol. 44, pp. 722–729, May 1996.

[6] ——, "Forward-backward method for scattering from imperfect conductors," *IEEE Trans. Antennas Propagat.*, vol. 46, pp. 101–107, Jan. 1998.

[7] M. Rodriguez Pino, L. Landesa, J. L. Rodriguez, F. Obelleiro, and R. J. Burkholder, "The generalized forward-backward method for analyzing the scattering from targets on ocean-like rough surfaces," *IEEE Trans. Antennas Propagat.*, vol. 47, pp. 961–969, June 1999.

[8] D. Torrungrueng, H.-T. Chou, and J. T. Johnson, "A novel spectral acceleration algorithm for the computation of scattering from two-dimensional rough surfaces with the forward-backward method," in *USNC/URSI Radio Sci. Meeting: URSI Dig.*, Orlando, FL, July 1999, p. 154.

[9] D. A. Kapp and G. S. Brown, "A new numerical method for rough-surface scattering calculations," *IEEE Trans. Antennas Propagat.*, vol. 44, pp. 711–721, May 1996.

[10] P. Tran, "Calculation of the scattering of electromagnetic waves from a two-dimensional perfectly conducting surface using the method of ordered multiple interaction," *Waves Random Media*, vol. 7, pp. 295–302, 1997.

[11] J. T. Johnson and H. T. Chou, "Numerical studies of low grazing angle backscatter from 1-D and 2-D impedance surfaces," in *IEEE Geosci. Remote Sensing Symp.*, Nov. 1998, pp. 2295–2297.

[12] A. Ishimaru, "Experimental and theoretical studies on enhanced backscattering from scatterers and rough surfaces," in *Scattering in Volumes and Surfaces*, M. Nieto-Vesperinas and J. C. Dainty, Eds. Amsterdam, The Netherlands: North-Holland, 1990, pp. 1–15.

[13] J. T. Johnson, L. Tsang, R. T. Shin, K. Pak, C. H. Chan, A. Ishimaru, and Y. Kuga, "Backscattering enhancement of electromagnetic waves from two-dimensional perfectly conducting random rough surfaces: A comparison of Monte Carlo simulations with experimental data," *IEEE Trans. Antennas Propagat.*, vol. 44, pp. 748–756, May 1996.

[14] J. C. West and J. M. Sturm, "On iterative approaches for electromagnetic rough-surface scattering problems," *IEEE Trans. Antennas Propagat.*, vol. 47, pp. 1281–1288, Aug. 1999.

[15] L. B. Felsen and N. Marcuvitz, *Radiation and Scattering of Waves*. Englewood Cliffs, NJ: Prentice-Hall, 1973.

[16] G. Tyras, *Radiation and Propagation of Electromagnetic Waves*. New York: Academic, 1969.

Danai Torrungrueng (M'95) was born in Bangkok, Thailand. He received the B.S. degree in electrical engineering from Chulalongkorn University, Bangkok, Thailand, in 1993 and received the M.S. degree in electrical engineering from The Ohio State University (OSU), Columbus, in 1996, where he is currently pursuing the Ph.D. degree.

Since 1995, he has been with the Department of Electrical Engineering, ElectroScience Laboratory, OSU, as a Graduate Research Assistant. His research area includes method of moment techniques for the analysis of electrically large antennas, numerical analysis of half-space problems, rough surface scattering problems, and electromagnetic wave theory.

Hsi-Tseng Chou (M'98) was born in ChangHua, Taiwan, R.O.C, in 1966. He received the B.S. degree in electrical engineering from National Taiwan University, in 1988, and the M.S. and Ph.D. degrees in electrical engineering from The Ohio State University (OSU), Columbus, in 1993 and 1996, respectively.

Since 1998, he has been an Assistant Professor with OSU, and also recently joined the Department of Electrical Engineering, Yuan-Ze University, Chung-Li, Taiwan. He was with China Ryoden Co., Ltd. in 1990, and then was with the ElectroScience Laboratory (ESL), OSU, as a Graduate Research Associate from 1991 to 1996. He was then a Postdoctoral Researcher with the ESL/OSU in 1996. His current interests include antenna design, electromagnetic scattering, the development of asymptotic high-frequency techniques such as uniform geometrical theory of diffraction (UTD), novel Gaussian beam techniques in the application of reflector antenna analysis, and UTD-type solutions for periodic structures.

Dr. Chou was invited to attend the International Radio Science Institute (URSI) General Assembly in 1999 under the Young Scientist Award Scheme, and also received a best paper award from OSU-ESL in 1999. He has been a reviewer for IEEE ANTENNAS AND PROPAGATION and URSI *Radio Science*.

Joel T. Johnson (M'96) received the B.E.E degree from the Georgia Institute of Technology, Atlanta, in 1991, and the S.M. and Ph.D. degrees from the Massachusetts Institute of Technology, Cambridge, MA, in 1993 and 1996, respectively.

He is currently an Assistant Professor with the Department of Electrical Engineering and ElectroScience Laboratory, The Ohio State University (OSU). His research interests are in the areas of microwave remote sensing, propagation, and electromagnetic wave theory.

Dr. Johnson received the 1993 best paper award from the IEEE Geoscience and Remote Sensing Society, and was named an Office of Naval Research Young Investigator, National Science Foundation Career awardee, and PECASE award recipient in 1997.